

Structurally Triggered Metal-Insulator Transition in Rare-Earth Nickelates

Alain Mercy,¹ Jordan Bieder,^{1,2} Jorge Íñiguez,³ and Philippe Ghosez¹

¹Theoretical Materials Physics, Q-MAT, CESAM, University of Liège, B-4000 Liège, Belgium

²CEA DAM-DIF, F-91297 Arpaçon, France

³Department of Materials Research and Technology,
Luxembourg Institute of Science and Technology, L-4362 Esch/Alzette, Luxembourg

(Dated: October 16, 2018)

Rare-earth nickelates form an intriguing series of correlated perovskite oxides. Apart from LaNiO_3 , they exhibit on cooling a sharp metal-insulator electronic phase transition, a concurrent structural phase transition and a magnetic phase transition toward an unusual antiferromagnetic spin order. Appealing for various applications, full exploitation of these compounds is still hampered by the lack of global understanding of the interplay between their electronic, structural and magnetic properties. Here, we show from first-principles calculations that the metal-insulator transition of nickelates arises from the softening of an oxygen breathing distortion, structurally triggered by oxygen-octahedra rotation motions. The origin of such a rare triggered mechanism is traced back in their electronic and magnetic properties, providing a united picture. We further develop a Landau model accounting for the evolution of the metal-insulator transition in terms of the R cations and rationalising how to tune this transition by acting on oxygen rotation motions.

First synthesized in 1971 [1], rare-earth nickelates (RNiO_3 , with R = rare earth) are appealing for various applications [2, 3] and the possibility to tune their properties in epitaxial films and heterostructures [4] has recently fuelled an even larger interest [5–7]. RNiO_3 compounds belong to the family of perovskite oxides with a reference $Pm\bar{3}m$ cubic structure (Fig. 1a), nevertheless not directly observed. Apart for LaNiO_3 , which always keeps a metallic $R\bar{3}c$ phase and will not be further discussed here, all RNiO_3 adopt at reasonably high temperature a metallic $Pbnm$ orthorhombic phase [8]. This phase, rather ubiquitous [9] amongst perovskites with small Goldschmidt tolerance factor [8], t , corresponds to a distortion of the cubic structure arising from the appearance of (i) combined anti-phase rotations of the oxygen octahedra along the x and y directions, R_{xy} (Fig. 1b), with the same amplitude Q_R and (ii) in-phase ro-

tations of the oxygen octahedra along z , M_z (Fig. 1c), with amplitude Q_M .

In this phase, all Ni atoms are equivalent and formally in a Jahn-Teller active d^7 (likely $t_{2g}^6 e_g^1$ low spin) configuration. Surprisingly, although compatible with the $Pbnm$ symmetry, cooperative Jahn-Teller distortions do not appear. Instead, at a temperature T_{MI} which strongly evolves with the R cation (i.e with t) [10], RNiO_3 compounds exhibit an electronic metal-insulator transition (MIT), which was shown to be concurrent with a structural transition from $Pbnm$ to monoclinic $P2_1/n$ symmetry [11]. This symmetry lowering is accompanied with the appearance of a breathing distortion of the oxygen octahedra, B_{OC} (Fig. 1d), which alternatively expand and contract with amplitude Q_B , according to a rock-salt pattern. This gives rise to two types of Ni sites with long and short Ni-O bonds respectively.

At low temperature (100-200K), RNiO_3 compounds finally show a magnetic phase transition toward an unusual E'-type antiferromagnetic (AFM) spin order identified by a Bragg vector $\mathbf{q} = (1/4, 1/4, 1/4)$ in pseudocubic notation [11–13]. For large cations ($R = \text{Nd}$ and Pr), the Neel temperature $T_N = T_{MI}$ and the system goes directly from paramagnetic metal (PM-M) to AFM insulator (AFM-I). For smaller R cations, T_N is much lower than T_{MI} ; the two phase transitions are decoupled and the system goes through an intermediate paramagnetic insulating phase (PM-I).

The origin of the MIT has been widely debated in the literature [14–19]. It was sometimes interpreted as a charge disproportionation at Ni sites [20] : $2(d^7) \rightarrow d^8 + d^6$. However, the importance of Ni 3d – O 2p hybridization – i.e., transfer of electrons from O to Ni and formation of oxygen holes (\underline{L}) keeping Ni in a d^8 configuration (i.e., $d^{8-n} \approx d^8 \underline{L}^n$) – was evoked early on [15]. Nowadays, the MIT is usually viewed as a charge ordering of the type $2(d^8 \underline{L}^1) \rightarrow (d^8) + (d^8 \underline{L}^2)$ [17, 21, 22]. In this scenario, B_{OC} appears important to stabilise the charge ordering and open the gap. As suggested in Ref. [23] and confirmed from statistical correlation techniques [24], R_{xy} and M_z are also expected to play an active role. However, a complete picture linking electronic, structural and magnetic properties is yet to emerge.

Unlike recent theoretical studies which were focusing specifically on the electronic properties [17–19, 21], we investigate here self-consistently the electronic and struc-

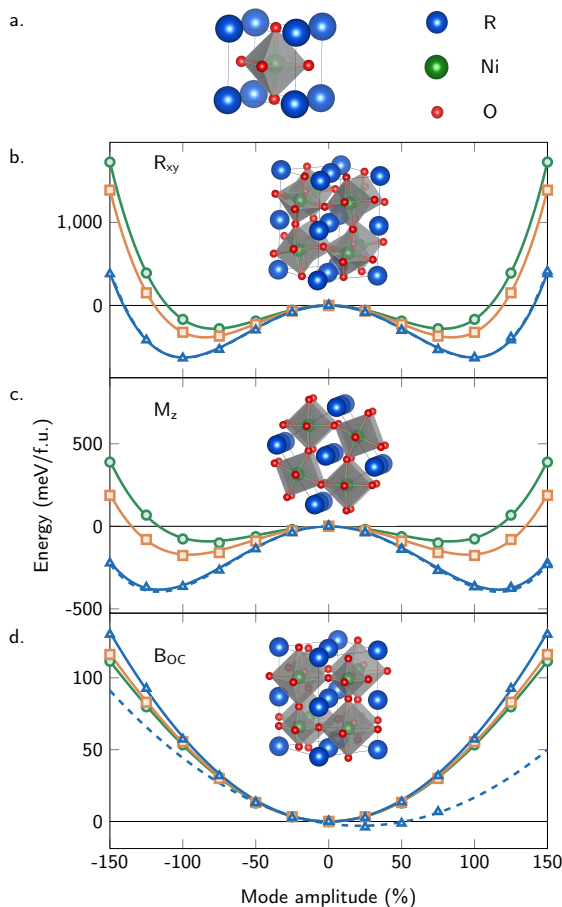


Figure 1: Reference cubic perovskite structure and most relevant atomic distortions. (a) Sketch of the reference $Pm\bar{3}m$ cubic perovskite cell of $RNiO_3$ compound with R at the corner, Ni at the centre and O atoms at the middle of the faces, forming corner-shared octahedra surrounding the B atoms. Starting from this reference, three main atomic distortions drive the system successively to the $Pbnm$ and then $P2_1/n$ phases : (b) anti-phase rotations of oxygen octahedra of same amplitudes about x and y axis (R_{xy}), (c) in-phase rotations of oxygen octahedra about z axis (M_z), (d) breathing of the oxygen octahedra (B_{OC}). The energy wells associated to the freezing of individual distortion of increasing amplitude in the cubic phase are shown for different R cations, associated to distinct tolerance factor t , and either a ferromagnetic (full line) or E'-type antiferromagnetic (dashed line, only for $R=Y$) spin arrangement : $YNiO_3$ ($t = 0.920$, blue), $GdNiO_3$ ($t = 0.938$, orange) and $SmNiO_3$ ($t = 0.947$, green). The atomic distortions are normalised to their amplitude in the $P2_1/n$ AFM-E' ground state of $YNiO_3$.

Calculations are done for each compound in a cubic phase that has the same volume as the ground state.

tural degrees of freedom of $RNiO_3$ compounds from density functional theory calculations (DFT, see Methods). Specific care was given to the validation of our approach, which turns out to provide an unprecedented agreement with experimental data. Focusing on $YNiO_3$, we show (see Supplementary S1) that not only the atomic structure but also the AFM-E' ground state, the estimated T_N and the electronic bandgap of the insulating phase are very accurately reproduced, making therefore our approach a method of choice to shed light on the interlink between these different features.

We start from the reference $Pm\bar{3}m$ cubic structure. Inspection of the phonon dispersion curves (see Supplementary S2) reveals dominant structural instabilities at R ($\omega_R = 310i \text{ cm}^{-1}$) and M ($\omega_M = 278i \text{ cm}^{-1}$) points of the Brillouin zone (BZ), which are associated respectively to the R_{xy} and M_z distortions responsible for the $Pbnm$ phase. These imaginary frequencies ω_i are linked to a negative energy curvature α_i at the origin ($\alpha_i \propto \omega_i^2 < 0$) and to a typical double-well (DW) shape of the energy when freezing R_{xy} and M_z distortions of increasing amplitude within the cubic structure, as illustrated in Fig. 1. These wells are nearly independent of the spin order but strongly evolve with the R cation : they become shallower when R size increases, consistently with a reduction of the related distortion amplitudes in the $Pbnm$ phase.

In contrast, the B_{OC} motion, corresponding to another phonon at R, is stable and extremely stiff (in fact the stiffest mode with $\omega_B = 700 \text{ cm}^{-1}$), in line with the single well (SW) shape illustrated in Fig. 1. Decreasing R -cation size tends to stabilise slightly further B_{OC} , in apparent contradiction with the observed increase of T_{MI} . As illustrated for $YNiO_3$, switching from ferromagnetic (FM) to AFM-E' spin order reduces slightly the curvature but does not reverse it; instead it shifts the SW to lower energy [13], yielding a finite Q_B at the minimum. Although B_{OC} tends to make the system insulating, this amplitude (25% of ground-state's value) is however not large enough to open a gap (more than 75% would be required). This shows that B_{OC} and the magnetic order only cannot explain the MIT by themselves.

Our central result is presented in Fig. 2 where we report the evolution of the B_{OC} energy well of $YNiO_3$ at various fixed amplitudes of oxygen rotation motions. It highlights that, although initially stable (SW), B_{OC} is progressively destabilized (DW) by the appearance of R_{xy} and M_z . As illustrated in the inset, α_B is renormalized into $\tilde{\alpha}_B$ which evolves linearly with Q_R^2 and Q_M^2 . The slope associated to Q_R is twice as large as that related to Q_M , attesting that each of the three individual rotations similarly affects B_{OC} . This behavior arises from the presence in the energy expansion of cooperative ($\lambda < 0$) bi-quadratic coupling terms between B_{OC} and oxygen rotations ($E \approx \lambda_{Bi} Q_B^2 Q_i^2$, $i = R, M$) which, being the lowest-order couplings al-

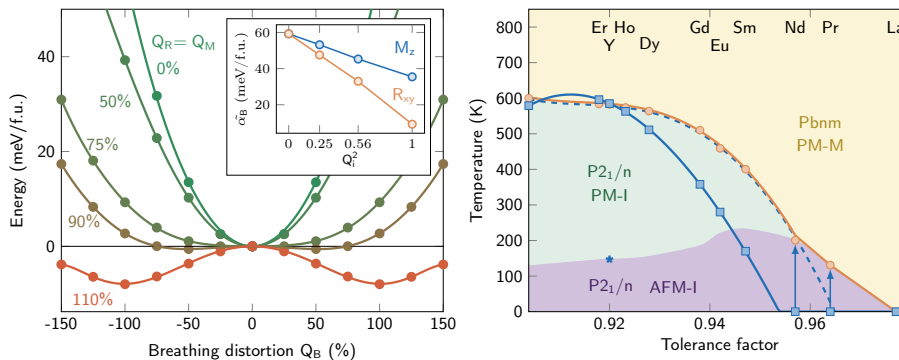


Figure 2: **Triggered mechanism and nickelate phase diagram** (a) Evolution of the energy E in terms of the amplitude of the breathing distortion (Q_B) for fixed amplitudes of oxygen rotations ($Q_R = Q_M$ from 0% to 110%) in the FM cubic phase of YNiO_3 (same volume as the ground state). It highlights the softening of the energy well associated to B_{OC} , triggered by the oxygen rotations R_{xy} and M_z . Inset : Linear evolution of the energy curvature at the origin, $\tilde{\alpha}_B$ along Q_B , in terms of the square of the amplitude of the individual distortions Q_R (orange) and Q_M (blue). (b) Phase diagram of $R\text{NiO}_3$ compounds in terms of their tolerance factor t and the temperature T . It includes 3 phases : a metallic $Pbnm$ paramagnetic phase (PM-M, yellow area), an insulating $P2_1/n$ paramagnetic phase (PM-I, green area) and an insulating $P2_1/n$ E'-type AFM phase (AFM-I, magenta area). The yellow line and dots show the experimental evolution of T_{MI} with the tolerance factor t . The blue line and squares is the prediction of the simple Landau model fitted on the first-principles data (FM order). The dashed blue line is the fit of the Landau expression of $T_{MI}(t)$ on experimental data. The blue star is the magnetic phase transition predicted for YNiO_3 from first-principles. The blue arrows indicate the correction to be applied on T_{MI} for large cations when properly incorporating the change of magnetic order.

lowed by symmetry, should give rise to the appearance of B_{OC} through a "triggered" phase transition according to Holakovsky [25]. The same behavior is observed independently of the magnetic order (see Supplementary S3). From now we focus on representative FM results while coming back to the role of magnetism later.

To further assess the relevance of such a triggered mechanism in nickelates, we built a Landau model including R_{xy} , M_z and B_{OC} degrees of freedom [24], restricting to lowest coupling terms and assuming temperature dependence of the oxygen rotations only :

$$\begin{aligned}
 E = & \gamma_R(T - T_{0R})Q_R^2 + \beta_R Q_R^4 + \lambda_{BR}Q_B^2 Q_R^2 \\
 & + \gamma_M(T - T_{0M})Q_M^2 + \beta_M Q_M^4 + \lambda_{BM}Q_B^2 Q_M^2 \\
 & + \alpha_B Q_B^2 + \beta_B Q_B^4 + \lambda_{MR}Q_M^2 Q_R^2.
 \end{aligned} \quad (1)$$

Within this model, R_{xy} and M_z appear at T_{0R} and T_{0M} . On cooling, they progressively develop within the $Pbnm$ phase and renormalize the energy curvature α_B of B_{OC} as made clear when grouping the Q_B^2 terms in Eq. (1):

$$\tilde{\alpha}_B = \alpha_B + \lambda_{BM}Q_M^2 + \lambda_{BR}Q_R^2 \quad (2)$$

When reaching a critical amplitude at which $\tilde{\alpha}_B = 0$, they trigger the appearance of B_{OC} and produce concurrent structural and metal-insulator phase transitions. The phase transition appears to be second order within this model, which is however too simple to be conclusive on this point (see Supplementary S3).

All parameters and their evolution with R were directly fitted from first-principles; only Curie temperatures were

uniformly scaled to reproduce the experimental T_{MI} of YNiO_3 (see Supplementary S3). The phase diagram of nickelates as predicted within this model is reported in Fig. 2. This figure demonstrates that the cooperative coupling of B_{OC} with R_{xy} and M_z is a key mechanism that, by itself, accounts for the experimentally observed evolution of T_{MI} with the tolerance factor.

Hence, the MIT in nickelates turns out to be a concrete example of triggered phase transition[26, 27], a kind of transition never identified before in simple perovskites. Indeed, although bi-quadratic interactions are generic in this class of compounds, different distortions usually compete and exclude each other [9]. The cooperative coupling of B_{OC} with oxygen rotations pointed out here is therefore an unusual and intriguing feature, whose origin is now traced back in the electronic band structure.

In the cubic phase, as expected from the formal $\text{Ni } 3d^7$ ($t_{2g}^6 e_g^1$) occupancy, the Fermi energy E_f crosses levels of dominant Ni $3d-e_g$ character (i.e. anti-bonding Ni $3d-O$ $2p$ states); such levels form an isolated and rather dispersive set of two e_g bands, shifted above the t_{2g} levels by the crystal field (Fig. 3). Forcing into this cubic structure a B_{OC} distortion, associated to a phonon at $\mathbf{q}_R = (1/2, 1/2, 1/2)$, can open a gap at $\mathbf{q}_c = (1/4, 1/4, 1/4)$ within the e_g bands but well above E_f and without any direct impact on the metallic character and the occupied states. Nevertheless, the oxygen rotation motions substantially affect the e_g bands (Fig. 3), reducing their bandwidth and yielding a progressive down shift of the

e_g levels at \mathbf{q}_c . As the rotations gradually increase and the bandwidth decreases, B_{OC} more substantially pushes down the electronic states around E_f , providing a progressive gain of electronic energy which, in turn, results in the softening of ω_B . The critical rotation amplitude at which B_{OC} becomes unstable ($\tilde{\alpha} = 0$) is precisely that at which the e_g levels at \mathbf{q}_c cross E_f . At these amplitudes, the electronic system itself becomes unstable; the appearance of B_{OC} is favored and opens a gap precisely at E_f , making the system insulating. As such, the MIT can therefore be interpreted as a Peierls instability but one that is not initially present and has been triggered by oxygen rotations.

For compounds with small R cations, Q_R and Q_M are large and able to produce the MIT at relatively high temperatures, well above T_N . For large cations ($R = \text{Nd, Pr}$), oxygen rotations are reduced and, from our Landau model (built on FM results), no more sufficient to trigger the MIT (Figure 2b). However, as previously mentioned, the AFM-E' spin order is compatible by symmetry with B_{OC} and induces its appearance as an improper order (linear shift of B_{OC} SW, Fig. 1d). Hence, although not opening a gap in the cubic phase, the onset of the AFM-E' order in the $Pbnm$ phase of NdNiO_3 and PrNiO_3 promotes the occurrence of the MIT almost triggered by the rotations. In these compounds, we have therefore $T_{MI} = T_N$; the transition is more abrupt and first-order [8]. Such active role of magnetism for large cations is supported by the experimental results and discussion in Ref. [28]. It is also confirmed by our first-principles calculations on NdNiO_3 , showing that the predicted T_{MI} is rescaled when including the change of magnetic order: while the system prefers to stay in the $Pbnm$ metallic phase when imposing a FM order, it switches to the $P2_1/n$ phase when adopting a AFM-E' order. The cooperative effect of the magnetic order remains true for small cations but without any impact on T_{MI} ($> T_N$).

In conclusion, the concurrent electronic and structural transitions at T_{MI} in $R\text{NiO}_3$ compounds take the form of a Peierls instability which, primarily, is structurally triggered by the oxygen rotation motions R_{xy} and M_z and, eventually, is further assisted by the appearance of the E'-type AFM magnetic ordering. Our Landau model, and its possible extension to incorporate explicitly strain degrees of freedom neglected here for simplicity, provides a simple and useful quantitative tool to estimate and interpret how T_{MI} can be tuned toward the monitoring of oxygen rotation motions R_{xy} and M_z when making solid-solutions [10], applying pressure [8] or playing with the epitaxial strain and the orientation of the substrate in thin films [29]. Our findings are relevant to other families of perovskites like $A^{2+}\text{Fe}^{4+}\text{O}_3$ compounds [30]. For instance, they can explain why CaFeO_3 , which exhibits oxygen rotations, undergoes a MIT while SrFeO_3 and BaFeO_3 , which stay cubic, remain metallic. In addition, the same physics is also inherent to manganites like

LaMnO_3 , suggesting a close competition between charge and orbital orderings in this family compounds. However, the situation is slightly different in bismutate like BaBiO_3 , in which B_{OC} is intrinsically unstable in the cubic phase [31].

METHODS

First-principles calculations were performed in the framework of Density Functional Theory (DFT) [32, 33] using a Projected Augmented Wave (PAW) approach [34] as implemented within the ABINIT package [35–38]. The calculations relied on the Generalized Gradient Approximation using the PBEsol [39] exchange-correlation functional. We worked within a collinear spin approximation. We included a Hubbard correction $U = 1.5$ eV [40] on the $3d$ orbitals of Ni atoms. A special care has been devoted to the determination of the appropriate U parameter (see Supplementary, Section S1).

We made use of JTH atomic potentials [41]. For the wave-functions, we used an energy cutoff of 24 Ha (38 Ha for the second grid in the PAW spheres), which guarantees a convergence better than 1 meV on the total energy. The Brillouin-zone was sampled with k -point meshes equivalent to a $12 \times 12 \times 12$ grid in the 5-atoms unit cell. During structural relaxations, thresholds of 10^{-5} Ha/bohr on the maximum force and of 10^{-7} Ha/bohr³ on the maximum stress have been considered.

The Goldschmidt tolerance factor, [42], $t = d_{R-O}/\sqrt{2}d_{Ni-O}$, of $R\text{NiO}_3$ compounds were determined using Nicole Benedek's tool [43] relying on a bond valence model [44] to calculate d_{R-O} and d_{Ni-O} , respectively the ideal R -O and Ni-O bond lengths in the cubic perovskite structure.

Symmetry-adapted mode analysis have been performed with AMPLIMODE [45, 46]. The modes are normalized to their amplitude in the $P2_1/n$ AFM-E' ground state. This normalization is such that in cubic phase (volume of the ground state) $Q_R = 100\%$ corresponds to rotation angles $\phi_x = \phi_y = 11.33^\circ$ (Ni-O-Ni angle of 157.33°), $Q_R = 100\%$ corresponds to a rotation angle $\phi_z = 12.12^\circ$ (Ni-O-Ni angle of 155.75°) and $Q_B = 100\%$ corresponds to oxygen displacements $d_O = 0.0358$.

The Landau model parameters have been fitted for YNiO_3 , GdNiO_3 and SmNiO_3 on first-principles data using in each case a FM cubic phase (volume of the ground state) and interpolated for the other compounds. T_{MI} was determined analytically (see Supplementary, Section S3).

SUPPLEMENTARY INFORMATION

Supplementary Information is available in the online version of the paper.

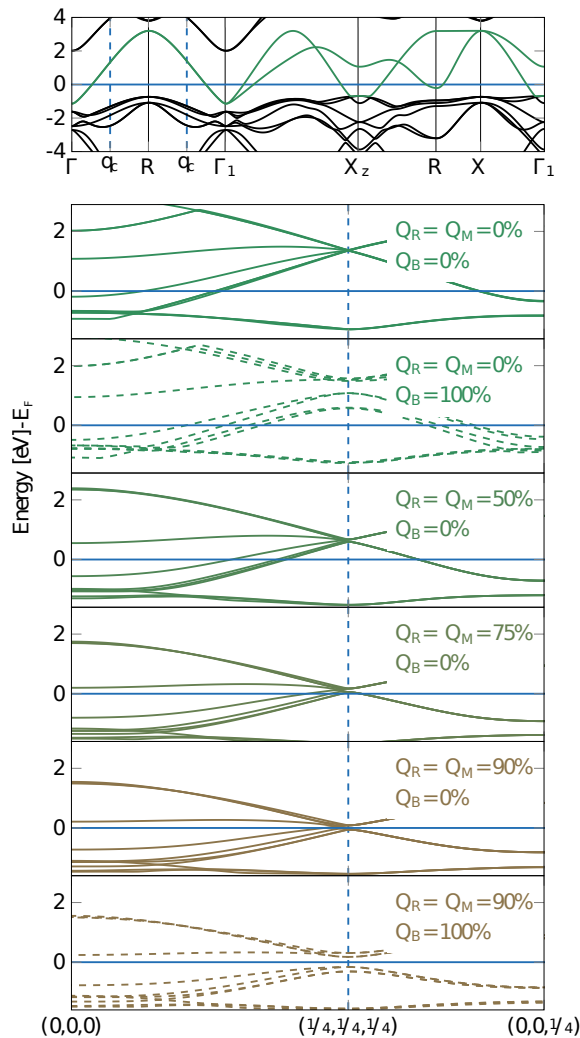


Figure 3: **Electronic properties** a. Electronic dispersion curves of YNiO_3 along different high symmetry line of the Brillouin zone of the $Pm\bar{3}m$ phase (FM case, majority spins): $\Gamma = (0, 0, 0)$, $X = (1/2, 0, 0)$, $M = (1/2, 1/2, 0)$ and $R = (1/2, 1/2, 1/2)$. The Ni 3d e_g bands are highlighted in green. The Fermi energy corresponds to the horizontal blue line. The point $q_c = (1/4, 1/4, 1/4)$ is located by vertical dashed blue lines. (b) Evolution of the electronic dispersion curves around the Fermi energy E_f (FM order, majority spins) when freezing into the $Pm\bar{3}m$ phase increasing amplitudes of oxygen rotations ($Q_R = Q_M$ from 0% to 90%, lines) and eventually adding the breathing distortion ($Q_B = 100\%$, dashed lines). The graph connects high-symmetry points (coordinates in pseudocubic notations) in the Brillouin zone of the $Pbnm$ or $P2_1/n$ 20-atom cell, in which bands have been folded respect to (a).

ACKNOWLEDGEMENTS

The authors thank Y. Zhang, E. Bousquet, F. Ricci, M. Verstraete, J.-Y. Raty, S. Catalano and J. Varignon for fruitful discussions. This work was supported by FRS-FNRS project HiT4FiT and ARC project AIMED. J.I. acknowledges support from FNR Luxembourg Grant P12/4853155 "COFERMAT". Calculations have been performed on the Céci facilities funded by F.R.S-FNRS (Grant No 2.5020.1) and Tier-1 supercomputer of the Fédération Wallonie-Bruxelles funded by the Walloon Region (Grant No 1117545). They also took advantage of HPC resources from the French Research and Technology Computing Center (CCRT) and from the PRACE project Megapasta.

- [1] Demazeau, G., Marbeuf, A., Pouchard, M. & Hagenmuller, P. Sur une série de composés oxygènes du nickel trivalent dérivés de la perovskite. *J. Solid State Chem.* **3**, 582 (1971).
- [2] Shi, J., Ha, S. D., Zhou, Y., Schoofs, F. & Ramanathan, S. A correlated nickelate synaptic transistor. *Nature Communications* **4**, 2676 (2013).
- [3] Zhou, Y. *et al.* Strongly correlated perovskite fuel cells. *Nature* **534**, 231–234 (2016).
- [4] Middey, S. *et al.* Physics of Ultrathin Films and Heterostructures of Rare-Earth Nickelates. *Annual Review of Materials Research* **46**, 305–334 (2016).
- [5] Först, M. *et al.* Spatially resolved ultrafast magnetic dynamics initiated at a complex oxide heterointerface. *Nature Materials* **14**, 883–888 (2015).
- [6] Kim, T. H. *et al.* Polar metals by geometric design. *Nature* **533**, 68–72 (2016).
- [7] Grisolia, M. N. *et al.* Hybridization-controlled charge transfer and induced magnetism at correlated oxide interfaces. *Nature Physics* **12**, 484–492 (2016).
- [8] Catalan, G. Progress in perovskite nickelate research. *Phase Transitions* **81**, 729–749 (2008).
- [9] Benedek, N. A. & Fennie, C. J. Why are there so few perovskite ferroelectrics? *The Journal of Physical Chemistry C* **117**, 13339–13349 (2013). <http://dx.doi.org/10.1021/jp402046t>.
- [10] Medarde, M. L. Structural, magnetic and electronic properties of RNiO_3 perovskites (R = rare earth). *Journal of Physics: Condensed Matter* **9**, 1679 (1997).
- [11] Alonso, J. A. *et al.* Charge Disproportionation in RNiO_3 Perovskites: Simultaneous Metal-Insulator and Structural Transition in YNiO_3 . *Physical Review Letters* **82**, 3871–3874 (1999).
- [12] García-Muñoz, J. L., Rodríguez-Carvajal, J. & Lacorre, P. Neutron-diffraction study of the magnetic ordering in the insulating regime of the perovskites RNiO_3 (R = Pr and Nd). *Physical Review B* **50**, 978–992 (1994).
- [13] Lee, S., Chen, R. & Balents, L. Landau Theory of Charge and Spin Ordering in the Nickelates. *Physical Review Letters* **106**, 016405 (2011).
- [14] Torrance, J. B., Lacorre, P., Nazzari, A. I., Ansaldo, E. J. & Niedermayer, C. Systematic study of insulator-metal

- transitions in perovskites $RNiO_3$ ($R = Pr, Nd, Sm, Eu$) due to closing of charge-transfer gap. *Physical Review B* **45**, 8209–8212 (1992).
- [15] Mizokawa, T., Khomskii, D. I. & Sawatzky, G. A. Spin and charge ordering in self-doped Mott insulators. *Physical Review B* **61**, 11263–11266 (2000).
- [16] Raebiger, H., Lany, S. & Zunger, A. Charge self-regulation upon changing the oxidation state of transition metals in insulators. *Nature* **453**, 763–766 (2008).
- [17] Park, H., Millis, A. J. & Marianetti, C. A. Site-Selective Mott Transition in Rare-Earth-Element Nickelates. *Physical Review Letters* **109**, 156402 (2012).
- [18] Ruppen, J. *et al.* Optical spectroscopy and the nature of the insulating state of rare-earth nickelates. *Physical Review B* **92**, 155145 (2015).
- [19] Varignon, J., Grisolia, M. N., Íñiguez, J., Barthélémy, A. & Bibes, M. Reconciling the ionic and covalent pictures in rare-earth nickelates. *arXiv:1603.05480 [cond-mat]* (2016). ArXiv: 1603.05480.
- [20] Mazin, I. I. *et al.* Charge Ordering as Alternative to Jahn-Teller Distortion. *Physical Review Letters* **98**, 176406 (2007).
- [21] Johnston, S., Mukherjee, A., Elfimov, I., Berciu, M. & Sawatzky, G. A. Charge Disproportionation without Charge Transfer in the Rare-Earth-Element Nickelates as a Possible Mechanism for the Metal-Insulator Transition. *Physical Review Letters* **112**, 106404 (2014).
- [22] Bisogni, V. *et al.* Ground state oxygen holes and the metal-insulator transition in the negative charge transfer rare-earth nickelates. *Nature Communications* **7**, 13017 (2016). ArXiv: 1607.06758.
- [23] de la Cruz, F. P. *et al.* Possible common ground for the metal-insulator phase transition in the rare-earth nickelates $RNiO_3$ ($R = Eu, Ho, Y$). *Physical Review B* **66**, 153104 (2002).
- [24] Balachandran, P. V. & Rondinelli, J. M. Interplay of octahedral rotations and breathing distortions in charge-ordering perovskite oxides. *Physical Review B* **88**, 054101 (2013).
- [25] Holakovskiy, J. A new type of ferroelectric phase transition. *Phys. Stat. Sol. (b)* **56**, 615–619 (1973).
- [26] Flerov, I. N., Gorev, M. V., Voronov, V. N., Tressaud, A. & Grannec, J. Triggered phase transitions in $Rb_2KB^{3+}F_6(B^{3+}: Er, ho)$ elpasolites. *J. Solid State Chem.* **3**, 582 (1971).
- [27] Iwata, M., Zhao, C. H., Aoyagi, R., Maeda, M. & Ishibashi, Y. Splitting of triggered phase transition in $Bi_{4-x}La_xTi_3O_{12}$ mixed crystals. *Japanese Journal of Applied Physics* **46**, 5894 (2007).
- [28] Vobornik, I. *et al.* Electronic-structure evolution through the metal-insulator transition in $RNiO_3$. *Phys. Rev. B* **60**, R8426–R8429 (1999).
- [29] Catalano, S. *et al.* Tailoring the electronic transitions of $NdNiO_3$ films through (111)pc oriented interfaces. *APL Materials* **3**, 062506 (2015).
- [30] Akao, T. *et al.* Charge-ordered state in single-crystalline $CaFeO_3$ thin film studied by x-ray anomalous diffraction. *Phys. Rev. Lett.* **91**, 156405 (2003).
- [31] Structural phase diagram and electron-phonon interaction in $Ba_{1-x}K_xBiO_3$, author = Liechtenstein, A. I. and Mazin, I. I. and Rodriguez, C. O. and Jepsen, O. and Andersen, O. K. and Methfessel, M., journal = Phys. Rev. B, volume = 44, issue = 10, pages = 5388–5391, numpages = 0, year = 1991, month = Sep, publisher = American Physical Society, doi = 10.1103/PhysRevB.44.5388, url = <https://link.aps.org/doi/10.1103/PhysRevB.44.5388> .
- [32] Hohenberg, P. & Kohn, W. Inhomogeneous electron gas. *Phys. Rev.* **136**, B864–B871 (1964).
- [33] Kohn, W. & Sham, L. J. Self-consistent equations including exchange and correlation effects. *Phys. Rev.* **140**, A1133–A1138 (1965).
- [34] Blöchl, P. E. Projector augmented-wave method. *Phys. Rev. B* **50**, 17953–17979 (1994).
- [35] Gonze, X. *et al.* ABINIT: First-principles approach to material and nanosystem properties. *Computer Physics Communications* **180**, 2582–2615 (2009).
- [36] Gonze, X. *et al.* First-principles computation of material properties: the ABINIT software project. *Computational Materials Science* **25**, 478 – 492 (2002).
- [37] Gonze, X. *et al.* A brief introduction to the abinit software package .
- [38] Torrent, M., Jollet, F., Bottin, F., Zérah, G. & Gonze, X. Implementation of the projector augmented-wave method in the ABINIT code: Application to the study of iron under pressure. *Computational Materials Science* **42**, 337–351 (2008).
- [39] Perdew, J. P. *et al.* Restoring the density-gradient expansion for exchange in solids and surfaces. *Phys. Rev. Lett.* **100**, 136406 (2008).
- [40] Liechtenstein, A. I., Anisimov, V. I. & Zaanen, J. Density-functional theory and strong interactions: Orbital ordering in mott-hubbard insulators. *Phys. Rev. B* **52**, R5467–R5470 (1995).
- [41] Jollet, F., Torrent, M. & Holzwarth, N. Generation of Projector Augmented-Wave atomic data: A 71 element validated table in the XML format. *Computer Physics Communications* **185**, 1246–1254 (2014).
- [42] Goldschmidt, V. M. Die gesetze der krystallochemie. *Naturwissenschaften* **14**, 477–485 (1926).
- [43] Benedek, N. Tolerance factor calculator v0.2.1 .
- [44] Lufaso, M. W. & Woodward, P. M. Prediction of the crystal structures of perovskites using the software program spuds. *Acta Crystallogr. B* **57**, 725 (2001).
- [45] Orobengoa, D., Capillas, C., Aroyo, M. I. & Perez-Mato, J. M. *AMPLIMODES*: symmetry-mode analysis on the Bilbao Crystallographic Server. *Journal of Applied Crystallography* **42**, 820–833 (2009).
- [46] Perez-Mato, J. M., Orobengoa, D. & Aroyo, M. I. Mode crystallography of distorted structures. *Acta Crystallographica Section A* **66**, 558–590 (2010).
- [47] Alonso, J. A. *et al.* High-temperature structural evolution of $RNiO_3$ ($R = Ho, Y, Er, Lu$) perovskites: Charge disproportionation and electronic localization. *Physical Review B* **64** (2001).
- [48] Prosandeev, S., Bellaiche, L. & Íñiguez, J. Ab initio study of the factors affecting the ground state of rare-earth nickelates. *Physical Review B* **85**, 214431 (2012).
- [49] Muñoz, A., Alonso, J. A., Martínez-Lope, M. J. & Fernández-Díaz, M. T. On the magnetic structure of $DyNiO_3$. *Journal of Solid State Chemistry* **182**, 1982–1989 (2009).
- [50] Mercy, A., J., B. & Ghosez, P. Magnetic properties of $YNiO_3$. *unpublished* (2017).
- [51] Arima, T., Tokura, Y. & Torrance, J. B. Variation of optical gaps in perovskite-type 3 *d* transition-metal oxides. *Physical Review B* **48**, 17006–17009 (1993).

- [52] Perez-Cacho, J., Blasco, J., Garcia, J., Castro, M. & Stankiewicz, J. Study of the phase transitions in SmNiO_3 . *J. Phys.: Condens. Matter* **11**, 405 (1999).
- [53] Nikulina, I., Novojilova, M., Kaulb, A., Maiorovab, A. & S.N., M. Synthesis and transport properties study of $\text{Nd}_{1-x}\text{Sm}_x\text{NiO}_{3-\delta}$ solid solutions. *Materials Research Bulletin* **39**, 803 (2004).
- [54] Íñiguez, J., Ivantchev, S., Perez-Mato, J. M. & García, A. Devonshire-landau free energy of BaTiO_3 from first principles. *Phys. Rev. B* **63**, 144103 (2001).
- [55] Zhong, W., Vanderbilt, D. & Rabe, K. M. First-principles theory of ferroelectric phase transitions for perovskites: The case of BaTiO_3 . *Phys. Rev. B* **52**, 6301–6312 (1995).

– SUPPLEMENTARY INFORMATION –
**STRUCTURALLY TRIGGERED METAL-INSULATOR TRANSITION
 IN RARE-EARTH NICKELATES**

S1. VALIDATION OF THE DFT+U APPROACH

In order to assess the validity of our DFT+U approach and determine the appropriate U parameter, we have considered a wide range of possible values for U (from 0 to 8 eV) and have compared the computed structural, magnetic and electronic properties to experimental data.

The results are summarized below for YNiO₃ considered as a test case. In line with what was reported independently in Ref. [19], it appears that a DFT approach with a moderate U value of 1.5 eV provides for nickelates an unprecedented agreement with experimental data, combining accurate description not only of the structural but also of the magnetic and electronic properties. It therefore offers a robust and ideal framework for the study of the interplay between these properties.

A. Atomic structure

In Figure S1, we report the relative deviations respect to experimental data at low temperature [47] for the lattice parameters and atomic distortions in the E'-type AFM $P2_1/n$ phase of YNiO₃ in terms of the amplitude of the U parameter. The atomic distortions are those with respect to the $Pm\bar{3}m$ phase and are quantified from a symmetry-adapted mode analysis performed with AMPLIMODE [45, 46]. The labels of the modes that are allowed by symmetry in the $Pbnm$ and $P2_1/n$ phases and a brief description of the related atomic motions are reported in Table S1.

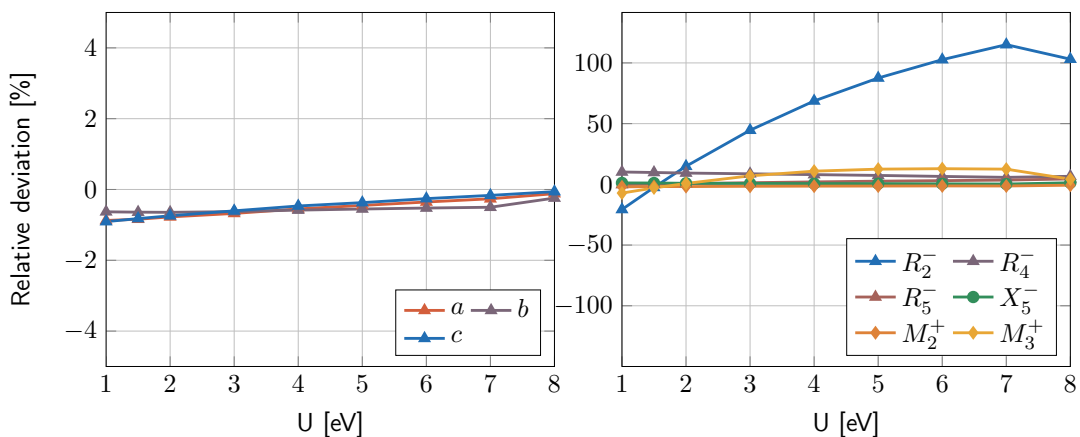


Figure 4: Relative deviations respect to experimental data at low temperature [47] for the lattice parameters (left panel) and atomic distortions (right panel) in the E'-type AFM $P2_1/n$ phase of YNiO₃ in terms of the amplitude of the U parameter. Atomic distortions are quantified from a symmetry-adapted mode analysis (see Table S1). The R_3^- and M_5^+ distortions which have negligible amplitudes (< 0.05) are not shown.

We see in Figure S1 that the lattice parameters are rather independent of U and well described within the whole range (error smaller than 1%). At the level of the atomic distortions, the amplitude of breathing mode B_{OC} (R_2^-) is only properly described in the limit of small U values. For the dominant modes like R_{xy} (R_5^-) or M_z (M_2^+), although the relative errors remain reasonably small for any U, the absolute amplitude evolves significantly with U and also converge to the correct values at low U.

In Figure S2, we report comparison with experiment data [47] of the absolute amplitudes of the atomic distortions and lattice parameters in the E'-type AFM $P2_1/n$ phase of YNiO₃ as computed in DFT with U = 1.5 eV. It confirms that the atomic structure of YNiO₃ is very accurately described in DFT using PBESol and a U parameter of 1.5 eV.

Labels	Atomic motion	<i>Pbnm</i>	<i>P2₁/n</i>
R_5^-	Anti-phase rotations of O octahedra along x and y (R_{xy})	x	x
M_2^+	In-phase rotations of O octahedra along z (M_z)	x	x
X_5^-	Anti-polar (layered) motion of R cations (X_{AP})	x	x
M_3^+	Jahn-Teller distortion of O octahedra (Q_2^+)	x	x
R_4^-	Anti-polar motion (rocksalt) of R cations (R_{AP})	x	x
R_2^-	Breathing distortion of the O octahedra (B_{OC})		x
M_5^+	Anti-polar motion of O (M_{AP})		x
R_3^-	Jahn-Teller distortion of O octahedra (Q_2^-)		x

Table I: Labels and description of the distortions of the $Pm\bar{3}m$ phase allowed by symmetry in the $Pbnm$ and $P2_1/n$ phases of $RNiO_3$ compounds. The main distortions are in bold.

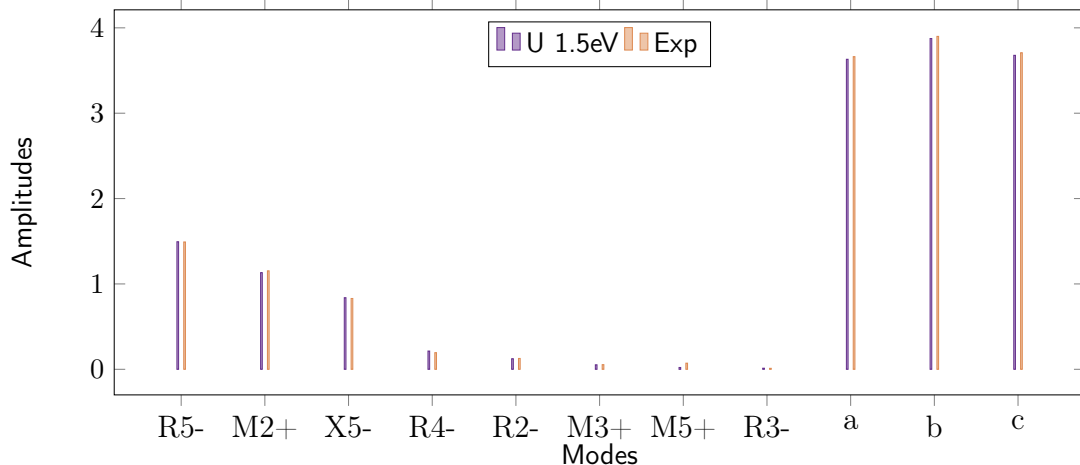


Figure 5: Comparison of the absolute amplitudes (Å) of the atomic distortions and lattice parameters in the E'-type AFM $P2_1/n$ phase of $YNiO_3$ as computed in DFT with $U = 1.5$ eV (purple) and as measured experimentally (orange). The E'-type AFM $P2_1/n$ ground state has a 80-atoms unit cell with lattice parameters $(a', b', c') = (2\sqrt{2}a, \sqrt{2}b, 4c)$.

B. Magnetic properties

In order to determine the magnetic ground state of the $P2_1/n$ phase of $YNiO_3$, we performed calculations for various magnetic orders associated to supercells of up to 80 atoms. While U values larger than 2 systematically favour a FM spin order, $U = 1.5$ eV properly stabilizes the E'-type spin ordering illustrated in Figure S3 as the ground state. It corresponds to an “up-up-down-down” spin arrangement related to a Bragg vector $\mathbf{q} = (1/4, 1/4, 1/4)$ in pseudocubic notations.

In our calculations, we get a magnetic moment $\mu = 1.2\mu_B$ on the Ni atoms associated to the large oxygen octahedra and $\mu \approx 0\mu_B$ on the Ni atoms associated to the small octahedra. This is similar with what has been reported in Ref. [19, 48] and in line with the $d^8 - d^8L^2$ picture [21]. It is also compatible with experimental data as discussed in Ref. [49].

Beyond the fact that DFT calculations with $U = 1.5$ eV provides the right magnetic ground state, it is interesting to check if it properly accounts for the strength of the magnetic interactions. To that end, we built a simple spin model $E_{mag} = (1/2) \sum J_{ij} S_i S_j$ including J_{ij} interactions up to fourth neighbours (6 independent parameters) and fitted the parameters on our first-principles data [50]. As illustrated in Figure S4 for $YNiO_3$ this spin model properly reproduces the energetics of the first-principles calculations.

Monte-Carlo simulations (using large boxes up to 1728 Ni atoms) from this spin-model [50] (i) confirmed the E'-type ground state and (ii) provided a Neel temperature $T_N = 154$ K, very similar to the mean-field estimate of 166 K and in close agreement with the experimental value of 150 K for $YNiO_3$ [11].

This demonstrates that our DFT calculations with $U = 1.5$ eV reproduces not only the correct E'-type magnetic ground state of nickelates but also properly describes the strength and anisotropy of their magnetic interactions.

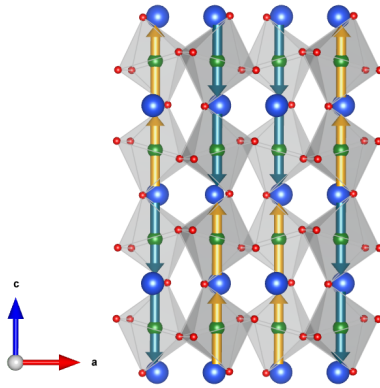


Figure 6: Spin order associated to the E'-type antiferromagnetic (AFM-E') ground state.

C. Electronic properties

Our DFT calculations with $U = 1.5$ eV properly accounts for the insulating character of the E'-type AFM $P2_1/n$ ground state of YNiO_3 . For the electronic bandgap, we get a value of 0.46 eV in reasonable agreement with the experimental estimate of 0.305 eV [51].

The electronic properties are further discussed in the manuscript. As it appears clearer there, the structural and electronic properties are intimately linked together in nickelates. Hence, the fact that our simulations describe accurately the structural properties of these compounds strongly suggests that they can also be trusted to investigate their electronic properties.

S2. PHONON DISPERSION CURVES

In Figure S5, we report the full phonon dispersion curves of the $Pm\bar{3}m$ phase of YNiO_3 , as calculated for a FM spin ordering at the volume of the $P2_1/n$ AFM-E' phase ($a_{pc} = 3.728\text{\AA}$). Similar curves have been obtained at the relaxed volume ($a_0 = 3.695\text{\AA}$). Interpolation of these phonon dispersion curves relies on the calculation of the interatomic force constants within a $2 \times 2 \times 2$ supercell. Although this might not be totally sufficient to get a fully converged interpolation, it provides already a good estimate of the shape of the dispersion curves. It is worth to notice that the frequencies at the high-symmetry points, which are the only ones discussed below and in the manuscript, are not interpolated but calculated explicitly within our approach.

On the one hand, the phonon dispersion curves highlight strong instabilities at the R and M q -points of the BZ, associated to the R_{xy} and M_z distortions. On the other hand, and quite amazingly, the breathing distortion, B_{OC} located at the R point, which finally produces the MIT, is associated to the hardest mode in the cubic phase. Clearly, such hard mode cannot spontaneously condense within the cubic structure.

We further notice the presence of two (triply-degenerated) unstable modes at Γ with very close frequencies. The softest one is associated to a polar-type motion involving R and O atoms; this kind of instability is expected for perovskites with small tolerance factors as YNiO_3 . The second one is the silent butterfly motion of the O atoms.

S3. LANDAU MODEL

Based on our DFT results, we have built a simple Landau-type model. In order to highlight the triggered mechanism, we restricted ourselves to the simplest possible model including only R_{xy} , M_z and B_{OC} degrees of freedom and lowest-order terms.

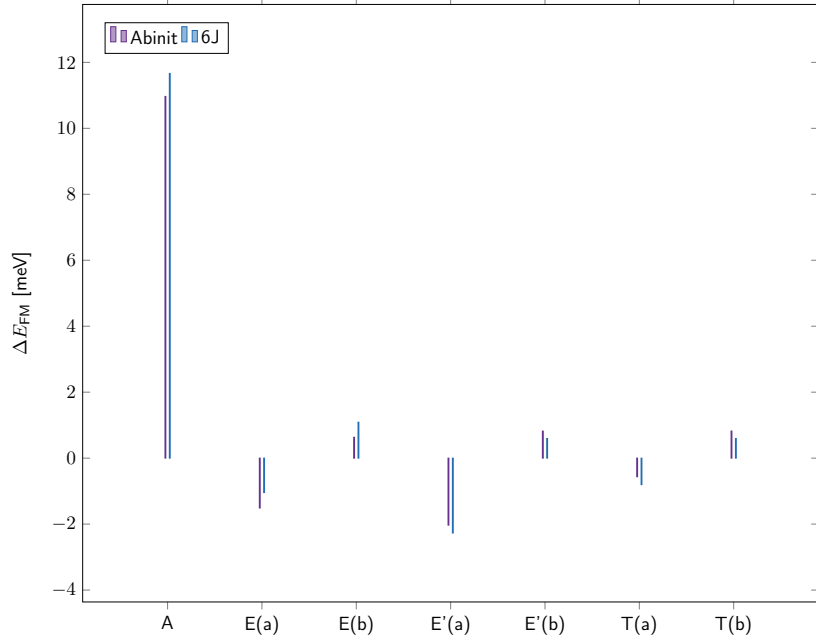


Figure 7: Comparison of the energy associated to various spin orders, respect to the FM order taken as reference, as obtained from our DFT calculations (purple) and simple spin model (blue). The A-type ordering corresponds to an antiferromagnetic stacking along the c direction of FM ordered ab planes. The E(a)-type order corresponds to an “up-up-down-down” zigzag chain along the a (orthorhombic) direction, and a FM order along the c direction. The E(b)-type order is characterised by the same “up-up-down-down” zigzag chain but along the b (orthorhombic) direction. The E'(a), E'(b), T(a) and T(b) types of order have the same in-plane properties too. However, the stacking along the c direction is different : E'(a) and E'(b) have two FM-order layers, AFM coupled with the next two layers while in the T(a) and T(b) configurations, the zigzag chain shifts about one spin along the chain direction at the same time one passes through the c direction. The ground state is E'(a) as illustrated in Figure S3 and simply called E' within the manuscript.

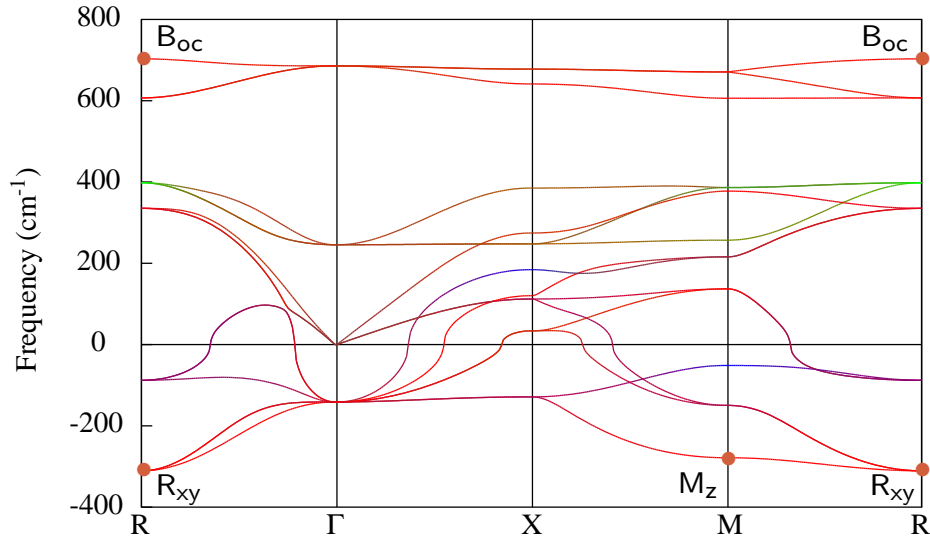


Figure 8: Phonon dispersion curve for the $Pm\bar{3}m$ phase of $YNiO_3$, at the $P2_1/n$ ground state volume and for a FM spin ordering ($U=1.5$ eV). Colors have been associated to the curves according to the involvement of each cation in the eigendisplacement of each mode (R in blue, Ni in green and O in red). Imaginary frequencies (unstable modes) appear as negative values.

Expression

Within our Landau-type model, the free energy in terms of the amplitudes Q_R , Q_M and Q_B (of R_{xy} , M_z and B_{OC} respectively) reads:

$$E(Q_M, Q_R, Q_B) = \alpha_R Q_R^2 + \beta_R Q_R^4 + \alpha_M Q_M^2 + \beta_M Q_M^4 + \alpha_B Q_B^2 + \beta_B Q_B^4 + \lambda_{MR} Q_M^2 Q_R^2 + \lambda_{MB} Q_M^2 Q_B^2 + \lambda_{RB} Q_R^2 Q_B^2 \quad (3)$$

The parameters α_R and α_M are assumed to be temperature dependent as

$$\alpha_R = \gamma_R(T_{0R} - T) \quad \text{and} \quad \alpha_M = \gamma_M(T_{0M} - T) \quad (4)$$

while all the other parameters are supposed to be constant.

Other modes allowed by symmetry (see Table S1) in the $Pbnm$ and $P2_1/n$ phases have not been explicitly included within the model. Some of them, like X_5^- (and to a lesser extent R_4^- and M_3^+), take however a significant amplitude and are crucial to stabilize the $Pbnm$ phase. They are implicitly included through a renormalization of the λ_{MR} parameter as it will appear more clearly in the next subsection.

The strain degrees of freedom have not been explicitly included within the model to highlight the key role of phonon-phonon couplings, which appear sufficient to reproduce experimental data on bulk compounds. However, this model could be naturally extended to strain degrees of freedom and their couplings with lattice modes. This might be useful to quantify for instance the role of epitaxial strain in thin films but is beyond the scope of this work.

The expansion has been limited to 4th order for all three order parameters including Q_B . This is justified by the fact that, from the fit of the parameters, the triggered transition appears to be second order. We notice however that explicit treatment of the strain (neglected here) could affect the order of the phase transition as further discussed below.

Fit from DFT

Parameters of our Landau-type model have been fitted on first-principles results. At first, we focused on YNiO_3 .

We considered in our calculations a fixed cubic $Pm\bar{3}m$ cell at a volume similar to that of the $P2_1/n$ AFM-E' ground-state ($a_{pc} = 3.728\text{\AA}$), which corresponds to imposing a negative strain of 0.9%. At this volume, relaxing within the $P2_1/n$ symmetry while keeping the unit cell fixed yields amplitudes of distortion comparable to the ground-state. We notice that, as illustrated in Fig. 9, similar calculations performed at the relaxed lattice constant ($a_0 = 3.695\text{\AA}$) yield very similar results. Even calculations performed while relaxing the lattice parameters at fixed mode amplitudes (in reduced coordinates) do not provide any significant change.

The calculations have been performed with a FM spin order which does not break any symmetry. We checked explicitly that the key physical features and conclusions (cooperative bi-quadratic coupling between rotations and breathing and triggered mechanism) remain similar for different AFM spin orders. The results remain even very similar in a non-magnetic (NM) calculation (with or without U correction) although, in that case, the amplitude of rotations required to destabilise B_{OC} is slightly larger ($\approx 160\%$); this last result illustrates that electronic Hund's rule energy, although playing a role, is not driving alone the appearance of B_{OC} as sometimes suggested [20].

The parameters of the Landau model at 0 K have then been extracted from DFT data as follows.

- $\alpha_R^0 (= \gamma_R T_{0R})$, $\alpha_M^0 (= \gamma_M T_{0M})$, β_R and β_M were fitted on the individual double wells associated to R_{xy} and M_z (Figure 1).
- λ_{RM} was fitted to reproduce the energy of a relaxed $Pbnm$ -like phase (full atomic relaxation while keeping the cubic cell fixed). From this, we renormalize the natural competition between R_{xy} and M_z by including implicitly the stabilising effect of X_5^- , R_4^- and M_3^+ modes. We notice that in all compounds, R_{xy} and M_z compete with each other and should yield $\lambda_{RM} > 0$. However, because of the renormalization due to the implicit presence of the other modes, λ_{RM} becomes negative for large cations (i.e. X_5^- helps stabilizing the $Pbnm$ phase consistently with the discussion in Ref. [9]).
- α_B was fitted on the single well associated to B_{OC} (Figure 1).
- λ_{BR} and λ_{BM} were fitted from the change of curvature of the well of B_{OC} when freezing 100% of Q_R and Q_M respectively (Figure 2).

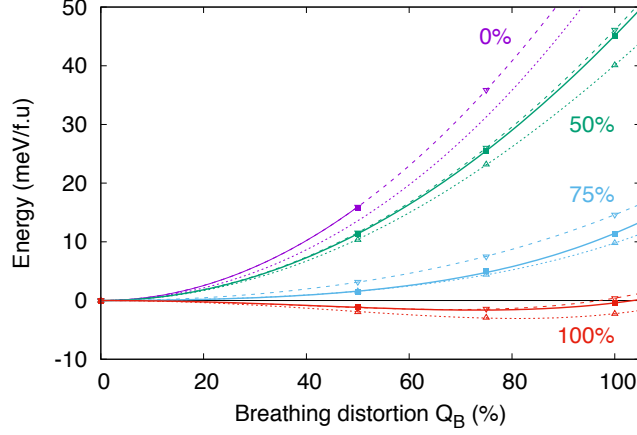


Figure 9: Evolution of the energy of YNiO_3 in terms of the amplitude of the breathing distortion for fixed amplitude of oxygen rotations ($Q_R = Q_M$, from 0% to 100%) in a FM configuration and either a fixed cubic cell (dotted line and triangles: $a_{pc} = 3.728 \text{ \AA}$; dashed line and back triangles: $a_0 = 3.695 \text{ \AA}$) or when relaxing fully the lattice parameters (full line and squares).

parameter	Y	Gd	Sm
t	0.920	0.938	0.947
α_B	58.1	52.6	50.6
β_B	10.0	16.0	31.0
α_M^0	-578.3	-385.5	-277.3
T_{0M}	3918	2571	1897
β_M	213.9	209.4	201.0
α_R^0	-1288.1	-1081.2	-920.9
T_{0R}	3918	3195	2833
β_R	648.8	754.9	750.4
λ_{MR}	31.8	-57.7	-99.4
λ_{MB}	-26.0	-29.0	-29.4
λ_{RB}	-35.8	-42.2	-42.4

Table II: Landau model parameters (meV/f.u. or K) as fitted on first-principles data, using the mode normalisation described in the Methods section.

- β_B was fitted to reproduce the right amplitude of B_{OC} in the ground state of the model and it was checked that the result still properly describes the single well associated to B_{OC} .

Within the model, the amplitude for the atomic distortion are renormalised to the one obtained from DFT calculation for the YNiO_3 ground state. This means 1 for rotation, tilts and breathing mode correspond to the amplitude of these modes in a cubic box with lattice parameters corresponding to 3.728 \AA .

We applied the same procedure to GdNiO_3 and SmNiO_3 . All the computed parameters are summarized in Table II.

As illustrated in Figure S6, all the parameters have an almost linear dependence in terms of the tolerance factor t . So, in our model, we assumed such a linear dependence to determine the value of the parameters at arbitrary t .

Finally, knowing $\alpha_{R,M}$ at 0 K (from the DFT calculations), their temperature dependence was estimated as follows. Focusing first on YNiO_3 we adjusted $T_{0R} = T_{0M}$ so that within our model, B_{OC} appears at the experimental value of 585K [8] and we deduced $\gamma_{M,R} = \alpha_{R,M}^0 / T_{0R,M}$: $\gamma_M = 0.148 \text{ meV/f.u.}$ and $\gamma_R = 0.331 \text{ meV/f.u.}$. Then, assuming $\gamma_{M,R}$ constant within the whole family the evolution of T_{0R} and T_{0M} with the tolerance factor were obtained as: $T_{0R,M} = \alpha_{R,M}^0 / \gamma_{M,R}$.

From this, we get the following final Landau-type expression for the free energy, allowing us to determine the values of Q_R, Q_M and Q_B for any value of the temperature T and tolerance factor t :

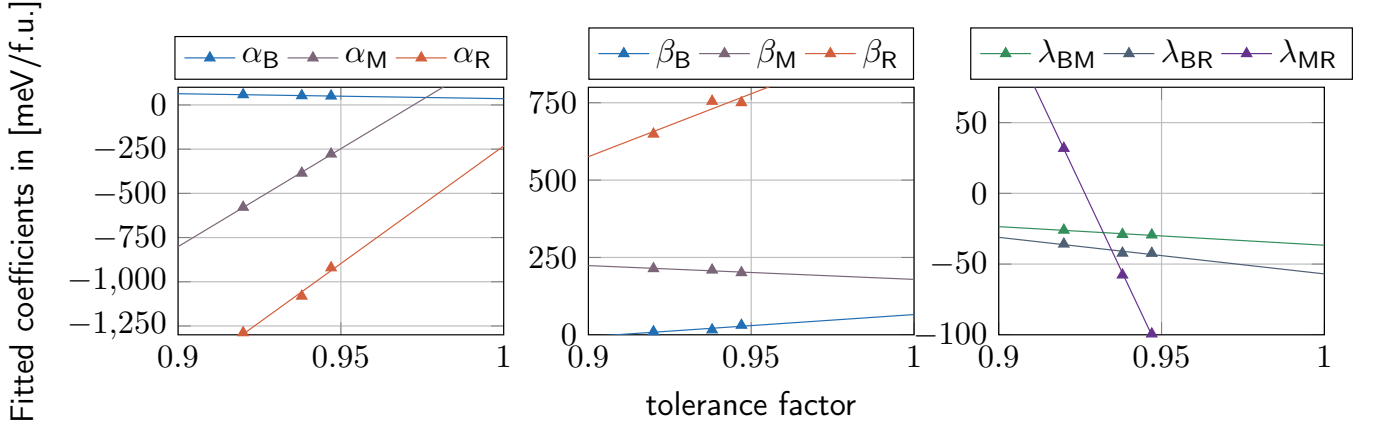


Figure 10: Evolution of the model parameters (meV/f.u.) with the tolerance factor.

$$\begin{aligned}
E(Q_M, Q_R, Q_B) = & \\
& (-281.9 \times t + 317.4)Q_B^2 + (714.3 \times t - 648.9)Q_B^4 \\
& - 0.15 \times (-74891.2 \times t + 72818.6 - T) \times Q_M^2 + (-446.3 \times t + 625.3) \times Q_M^4 \\
& - 0.33 \times (-40212.2 \times t + 40913.9 - T) \times Q_R^2 + (4067.9 \times t - 3085.5) \times Q_R^4 \\
& + (-4875.7 \times t + 4517)Q_M^2 Q_R^2 + (-131.6 \times t + 94.9) \times Q_M^2 Q_B^2 + (-258.6 \times t + 201.6) \times Q_R^2 Q_B^2
\end{aligned} \tag{5}$$

Analytical solution

From this model, T_{MI} can be determined analytically.

We start from the expression:

$$\begin{aligned}
E(Q_M, Q_R, Q_B) = & \alpha_B Q_B^2 + \beta_B Q_B^4 \\
& + \gamma_M \times (T_{0M} - T) \times Q_M^2 + \beta_M Q_M^4 \\
& + \gamma_R \times (T_{0R} - T) \times Q_R^2 + \beta_R Q_R^4 \\
& + \lambda_{MR} Q_M^2 Q_R^2 + \lambda_{MB} Q_M^2 Q_B^2 + \lambda_{RB} Q_R^2 Q_B^2
\end{aligned} \tag{6}$$

At the energy minimum, we should have :

$$\frac{\partial E}{\partial Q_M} = 0 \text{ and } \frac{\partial E}{\partial Q_R} = 0. \tag{7}$$

The solutions for that, other than $Q_M = 0$ and $Q_R = 0$, are :

$$\begin{aligned}
Q_M^2 = & \frac{-2T_{0M}\gamma_M\beta_R + T_{0R}\gamma_R\lambda_{MR} + T(2\gamma_M\beta_R - \gamma_R\lambda_{MR})}{4\beta_M\beta_R - \lambda_{MR}^2} \\
& + \frac{(-2\beta_R\lambda_{MB} + \lambda_{MR}\lambda_{RB})}{4\beta_M\beta_R - \lambda_{MR}^2} Q_B^2 \\
Q_R^2 = & \frac{-2T_{0M}\gamma_M\beta_R + T_{0R}\gamma_R\lambda_{MR} + T(2\gamma_M\beta_R - \gamma_R\lambda_{MR})}{4\beta_M\beta_R - \lambda_{MR}^2} \\
& + \frac{(-2\beta_R\lambda_{MB} + \lambda_{MR}\lambda_{RB})}{4\beta_M\beta_R - \lambda_{MR}^2} Q_B^2
\end{aligned} \tag{8}$$

Introducing this in Eq. (4) we get :

$$E(Q_B) = \alpha'_B Q_B^2 + \beta'_B Q_B^4 \tag{9}$$

where

$$\alpha'_B = \alpha_B + \frac{(\gamma_M \lambda_{MR} \lambda_{RB} - 2\gamma_M \beta_R \lambda_{MB})}{4\beta_M \beta_R - \lambda_{MR}^2} (T_{0M} - T) \quad (10)$$

$$+ \frac{(\gamma_R \lambda_{MB} \lambda_{MR} - 2\gamma_R \beta_M \lambda_{RB})}{4\beta_M \beta_R - \lambda_{MR}^2} (T_{0R} - T)$$

$$\beta'_B = \beta_B + \frac{\lambda_{MB} \lambda_{MR} \lambda_{RB} - \beta_M \lambda_{RB}^2 - \beta_R \lambda_{MB}^2}{4\beta_M \beta_R - \lambda_{MR}^2} \quad (11)$$

$$(12)$$

The MIT is linked to the appearance of the B_{OC} . This will appear at a temperature T_{MI} at which $\alpha'_B = 0$. This critical temperature is given by :

$$T_{MI} = \frac{\alpha_B(-4\beta_M \beta_R + \lambda_{MR}^2)}{2\gamma_M \beta_R \lambda_{MB} - \gamma_R \lambda_{MB} \lambda_{MR} + 2\gamma_R \beta_M \lambda_{RB} - \gamma_M \lambda_{MR} \lambda_{RB}} \quad (13)$$

$$+ \frac{T_{0R} \gamma_R (-\lambda_{MB} \lambda_{MR} + 2\beta_M \lambda_{RB})}{2\gamma_M \beta_R \lambda_{MB} - \gamma_R \lambda_{MB} \lambda_{MR} + 2\gamma_R \beta_M \lambda_{RB} - \gamma_M \lambda_{MR} \lambda_{RB}}$$

$$+ \frac{T_{0M} \gamma_M (2\beta_R \lambda_{MB} - \lambda_{MR} \lambda_{RB})}{2\gamma_M \beta_R \lambda_{MB} - \gamma_R \lambda_{MB} \lambda_{MR} + 2\gamma_R \beta_M \lambda_{RB} - \gamma_M \lambda_{MR} \lambda_{RB}}$$

Furthermore, supposing a linear dependence for all the coefficients with respect to the tolerance factor, we get a generic expression :

$$T_{MI} = \frac{a + t \times (b + (c + d \times t)t)}{e + t \times (f + g \times t)} \quad (14)$$

where t is the tolerance factor and a, b, c, d, e, f and g are a combination of model parameters.

Using the coefficients determined from DFT calculations in the previous Section, we can predict the evolution of T_{MI} as a function of the tolerance factor as illustrated in Figure 2b, blue line.

Independently, we can also fit the experimental data point using Eq. 13. Making such a fit, while excluding Nd and Pr compounds, we get the dashed blue line in Figure 2b.

Order of the transition

Experimentally, there is still some debate about the order of the MIT. For large cations ($T_{MI} = T_N$), the MIT is rather abrupt and hysteretic and unanimously considered as being first order [8]. The magnetic transition that takes place at the same temperature is also first order [28]. For small cations ($T_{MI} > T_N$), the MIT is less hysteretic and sometimes considered as evolving to second-order. Some studies seem however to show that it stays first-order [52, 53], while the less hysteretic behavior could be related to the fact that kinetics are better at higher temperatures [8]. For these compounds the magnetic transition is second-order.

As previously mentioned, the MIT is predicted to be second-order within our very simple model. As highlighted in Table S2, computed β_B is positive for all compounds. From Eq. 12, the oxygen rotations renormalize the fourth-order term coefficient and a negative value of β'_B would give rise to a first-order transition (it would then further require including 6th order terms in Q_B). Although this renormalization is negative, β'_B stays nevertheless positive in all cases ($\beta'_B = 9, 14$ and 29 respectively for $\text{YNiO}_3, \text{GdNiO}_3$ and SmNiO_3 respectively) corresponding therefore to a second-order transition.

Yet, we have to stress that our approach does not allow us to address the order of the transition conclusively. First, our model is built at fixed cubic cell and does not include strain relaxation. Explicit treatment of the latter will further renormalize the 4th-order term and might potentially make it negative, so eventually changing the order of the transition. Second, at a more fundamental level, even if our DFT+U results suggest that Q_B undergoes a second-order transition, that does not rule out the possibility that thermal effects effectively render a first-order transformation driven by temperature. The ferroelectric phase transitions of BaTiO_3 , a well studied case, are a concrete example of this [54], and also illustrate the critical role of strains to enhance the discontinuous character of the transformation [55]. Hence, discussing the character of the transition from first-principles would require explicitly statistical simulations that fall beyond of the scope of this work. The Landau model introduced here was kept simple on purpose in order to highlight the key role of the triggered mechanism and it show that, based on our first-principles results and a minimal experimental input, the main features of the phase diagram can be readily reproduced. Further, the main trends (regarding ionic size, amplitude of the different rotations, ...) are properly captured by this simple model, which moreover provides us with insights about how to tune the behaviour of these materials. In this sense, we consider that the proposed Landau model is valid and useful although, admittedly, it is not suitable for a definite discussion of the order of the transition.

For large cations (Nd and Pr), our model predicts that the MIT can no more be fully triggered by the oxygen rotations (which are reduced); for those compounds, it is complementarily promoted by the appearance of the AFM-E' magnetic order. In such case, the MIT takes place at $T_{MI} = T_N$; it is expected to be more abrupt and to be first order. Such coupling between the structural and magnetic transition for large cations is in line with the conclusions of Vobornik *et al.* in Ref. [28]: they suggest indeed that, contrary to other cases, there is a possible interplay between electronic and magnetic degrees of freedom when $T_{MI} = T_N$ and that any further model of the TMI should address that fact. Our manuscript explicitly addresses that point and we believe that it convincingly answers their questioning.

S4. ELECTRONIC BAND STRUCTURES

In Figure S6, we report the electronic dispersion curves of YNiO_3 with a FM spin order, along a more exhaustive path of the Brillouin zone of the $Pbnm$ or $P2_1/n$ 20-atom cell. The majority spins are in colors while the minority spins are in light grey. The latter have been omitted for clarity in the main manuscript. We notice that the cubic phase is essentially non magnetic (up and down spin bands nearly degenerate) and magnetism starts to develop with the rotations.

In Figure S7, we report similarly the electronic dispersion curves of YNiO_3 but with an AFM-A spin order. This figure is very similar to the previous one, demonstrating that our results are not dependent of the specific choice of spin order.

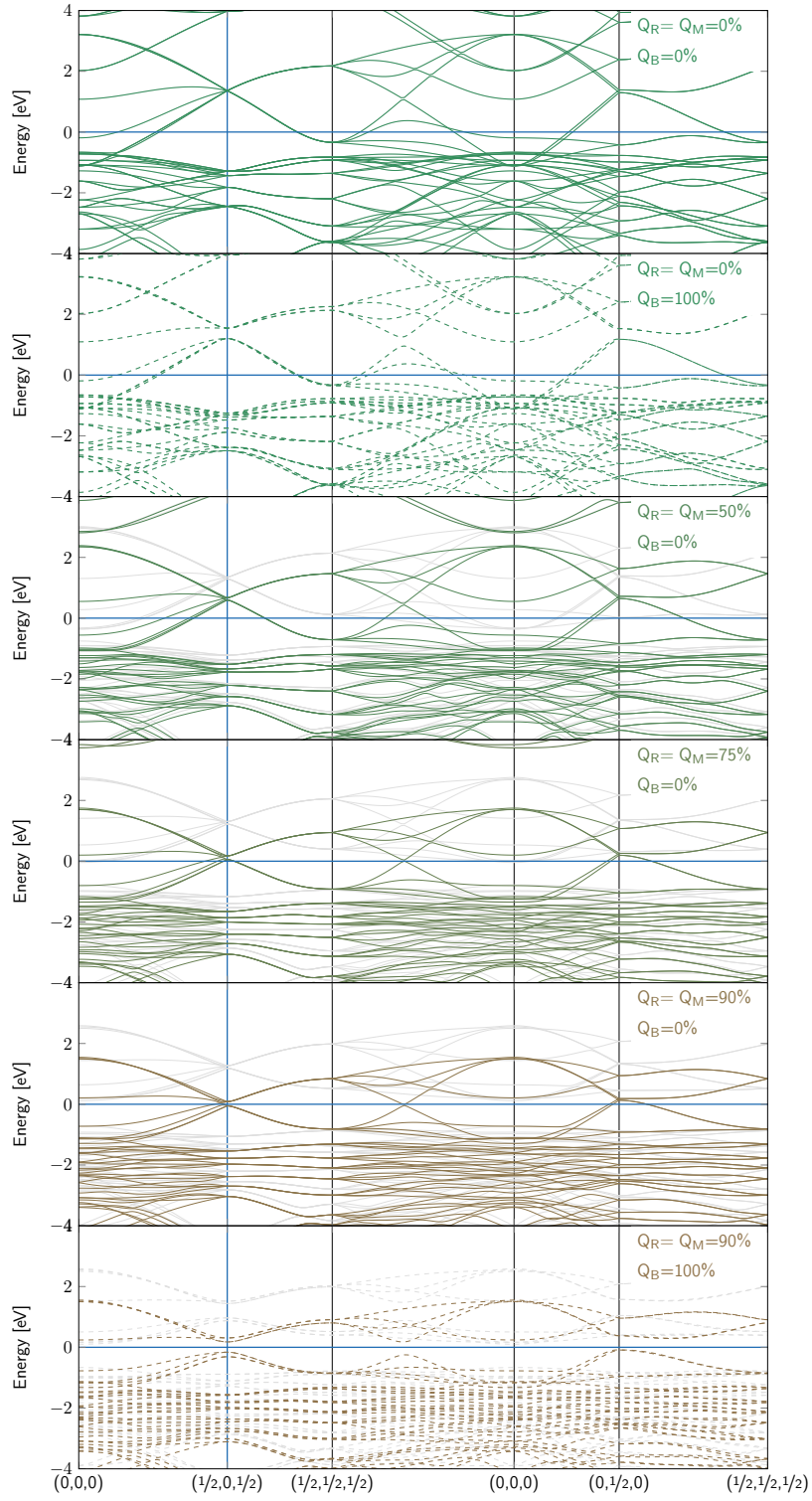


Figure 11: YNiO_3 , FM spin order. Evolution of the electronic dispersion curves around the Fermi energy E_f when freezing into the $Pm\bar{3}m$ phase increasing amplitudes of oxygen rotations ($Q_R = Q_M$ from 0% to 90%, lines) and eventually adding the breathing distortion ($Q_B = 100\%$, dashed lines). The graph connects high-symmetry points in the Brillouin zone of the $Pbnm$ or $P2_1/n$ 20-atom cell. Majority spins are in colors and minority spins in light grey.

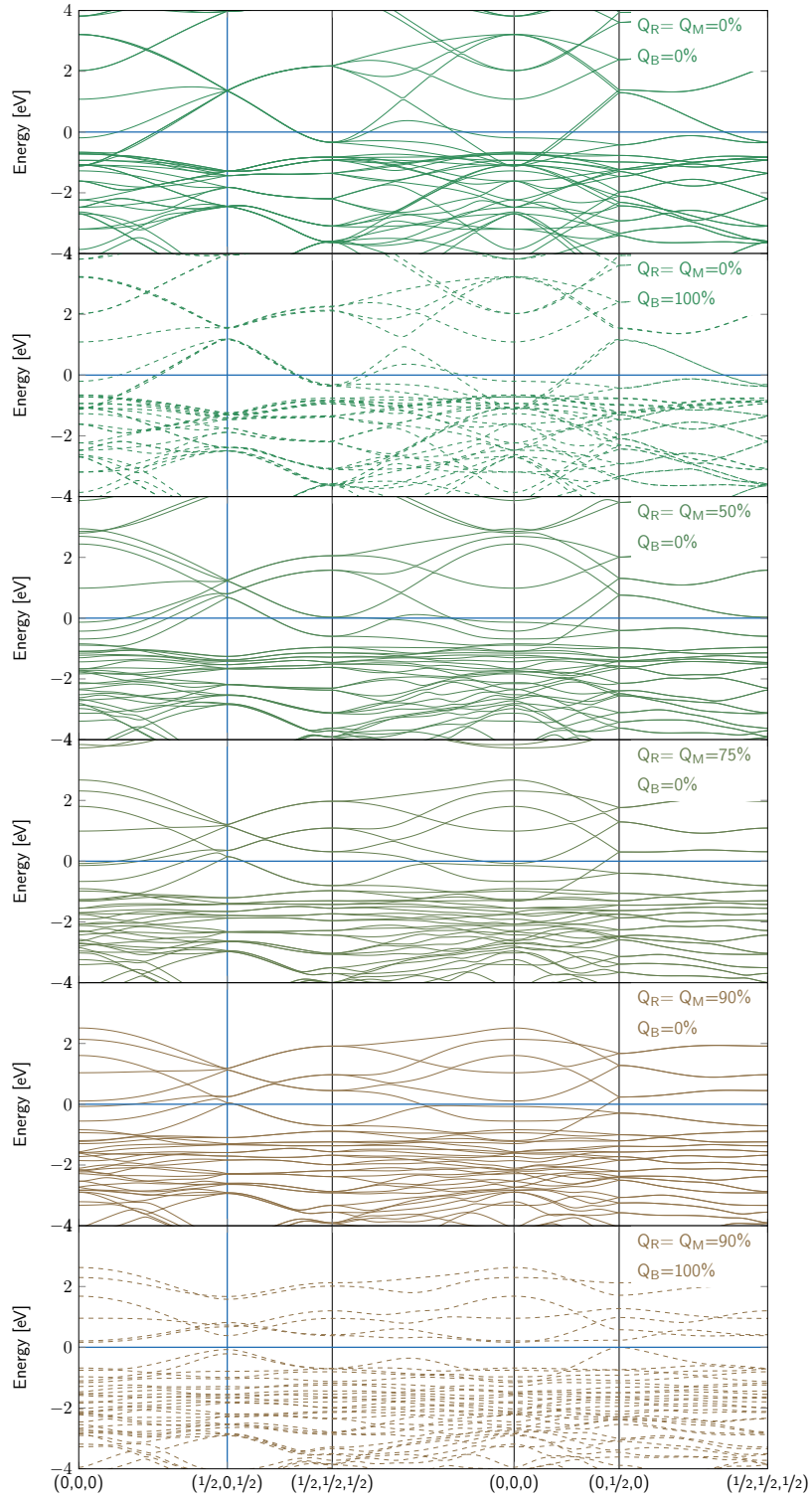


Figure 12: YNiO_3 , AFM-A spin order. Evolution of the electronic dispersion curves around the Fermi energy E_f when freezing into the $Pm\bar{3}m$ phase increasing amplitudes of oxygen rotations ($Q_R = Q_M$ from 0% to 90%, lines) and eventually adding the breathing distortion ($Q_B = 100\%$, dashed lines). The graph connects high-symmetry points in the Brillouin zone of the $Pbnm$ or $P2_1/n$ 20-atom cell.